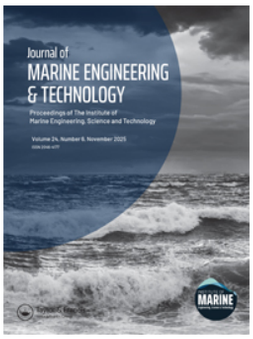

Taylor & Francis
Taylor & Francis Group

Journal of Marine Engineering & Technology

ISSN: 2046-4177 (Print) 2056-8487 (Online) Journal homepage: www.tandfonline.com/journals/tmar20

Field experiments on real-time autonomous marine surveillance

C. Fruzzetti, F. Ponzini, N. Sabatino, S. Donnarumma, R. Zaccone & M. Martelli

To cite this article: C. Fruzzetti, F. Ponzini, N. Sabatino, S. Donnarumma, R. Zaccone & M. Martelli (07 Apr 2026): Field experiments on real-time autonomous marine surveillance, Journal of Marine Engineering & Technology, DOI: 10.1080/20464177.2026.2648364

To link to this article: https://doi.org/10.1080/20464177.2026.2648364

Published online: 07 Apr 2026.

JOURNAL OF MARINE ENGINEERING & TECHNOLOGY
https://doi.org/10.1080/20464177.2026.2648364

Taylor & Francis
Taylor & Francis Group

Field experiments on real-time autonomous marine surveillance

C. Fruzzetti, F. Ponzini, N. Sabatino, S. Donnarumma, R. Zaccone and M. Martelli

Department of Naval Architecture, Electric, Electronic, and Telecommunication Engineering (DITEN), University of Genoa, Genoa, Italy

ABSTRACT

Monitoring and protecting critical marine infrastructures–such as offshore wind farms, data cables, and subsea pipelines–demands reliable, autonomous surface vessels capable of operating efficiently in real-world conditions. In these scenarios, the area of interest is typically known in advance, and the primary objective is to detect intruders or any other anomaly. This paper introduces a comprehensive Guidance, Navigation, and Control (GNC) architecture for Marine Autonomous Surface Ships (MASS), with particular emphasis on model-scale validation conducted during a relevant environmental testing campaign. The underlying hypotheses and methodologies are detailed and thoroughly discussed. Building on previous simulation-based studies that validated individual components, this work focuses on verifying the integration of the stochastic coverage planner, the tracking controller, and the state estimation subsystem through simulation and real-world field trials. The experimental results obtained from tests conducted at an outdoor site demonstrate successful completion of surveillance missions, real-time compliance, and the system's adaptability to dynamic changes and environmental disturbances. These findings confirm the feasibility of transferring complex autonomous behaviours from simulation to operational platforms. The proposed framework provides solid validation for future research and development of the architecture, enabling integration with the perception system and collision-avoidance capabilities to detect and avoid obstacles and intruders.

ARTICLE HISTORY
Received 11 May 2025
Accepted 14 March 2026

KEYWORDS
GNC; MASS; critical infrastructure surveillance; dark ship detection; coverage algorithm; situational awareness

1. Introduction

With the rise of containerisation and the emergence of the offshore oil & gas industry in the 1960s, the ocean has become a hub of economic activities, which have experienced an exponential growth in their output, both in terms of volume and in revenue. Nowadays, a relevant share of the fossil fuels being extracted worldwide comes from the seabed (Jouffray et al., 2020, Claire, 2016) and in the period from 1980 to 2022, the amount of container ship trade has quadrupled (UNCTAD, 2022), making maritime trading activities account for 80% of the global trade volume and 70% of its value (UNCTAD, 2017). Alongside trading and oil & gas extraction, new ocean-related economic activities have emerged in recent years, contributing to this economic boom. Among them, offshore wind farms and seabed cable-laying are expected to be the most prominent. Offshore wind farming is attracting many investments worldwide as a consequence of the global energy transition effort (Commission, 2023), while more than 95% of all data that moves around the world goes through undersea data cables, with a total of over 900,000 miles of cables sit on the ocean floor (Chataut, 2024), which are expected to increase in future years. This economic boom of ocean-related activities, driven among other things by the growing scarcity of land-based resources (Jouffray et al., 2020), is increasing the reliance of some industrial sectors and even whole countries on maritime infrastructures. These infrastructures can now be considered critical for ensuring proper energy and food security. Thus, the concept of Critical Maritime Infrastructure (CMI), proposed since the 1990s, is now a key factor in the strategic decision-making of many countries (Fritzon et al., 2007).

CMIs are notoriously susceptible to different sources of harm. Unintentional damage occurs, particularly during fishing activities (Clare, 2021). Additionally, deliberate attacks have been reported in recent years, disrupting energy sources or communication links (Bueger, 2023, Knights, 2024). Deliberate attacks represent a significant security challenge, as such acts are usually carried out by dark ships or shadow vessels (Kantchev, 2023), i.e. ships that cover their true activities by means of concealing techniques such as turning off their Automatic Identification System (AIS) device, spoofing their AIS location or using a flag of convenience (Nguyen, 2023).

Moreover, CMI protection presents distinct challenges relative to land-based critical infrastructure, owing to the difficulties of conducting operations at sea and extending them. Therefore, tailored solutions are required. One of the primary solutions is surveillance and monitoring. Thanks to recent advances in computing and communication technologies, this can be carried out effectively and efficiently using Maritime Autonomous Surface Ships (MASS) and Unmanned Underwater Vehicles (UUV) (Bueger and Liebetrau, 2023).

This article is the extension of the 2024 iSCSS conference proceeding (Ponzini et al., 2024). The original paper presents an integrated solution for real-time surveillance of CMIs based on a MASS platform. The architecture relies on the well-known Guidance, Navigation, and Control (GNC) systems (Fossen, 2011). Alongside these three systems, a fourth named shadow vessel monitoring system has been added to the platform and its aim is to detect intruding vessels that attempt to conceal their position. The platform is designed to surveil a known area and detect the presence of shadow vessels and other intruders using an onboard LiDAR. Compared with the original work, simulation and model-scale experiments have been conducted to validate the GNC architecture. The shadow vessel monitoring system has not been tested experimentally; however, it can

CONTACT C. Fruzzetti camilla.fruzzetti@unige.it Department of Naval Architecture, Electric, Electronic, and Telecommunication Engineering (DITEN), University of Genoa, Via Montallegro 1, Genoa, 16145, GE, Italy

be treated as an external module that can be integrated in different ways without compromising the overall framework. This extended version aims to present the validation of the proposed architecture through comprehensive tests in a relevant environment. Throughout the validation and investigation process, a MASS model of the SWAMP-class (Odetti et al., 2020) was employed; its architecture and key characteristics are discussed in detail in the following sections and it is deeply testes as shown inZaccone et al. (2026). To the best of the authors' knowledge, the current literature still lacks a comprehensive description of a surveillance platform based on small MASSs that integrates planning, navigation, control, and perception within a unified system architecture, as proposed in this work.

The rest of paper is organised as follows. In Section 2 related works are discussed. In Section 3 the system architecture of the autonomous surveillance platform developed for this paper is described, focusing on the input-output relations between its subsystems. In Section 4 the kinematics of the surveying MASS is described. In Sections 5, 6 and 7 the guidance, the control, and the navigation systems are discussed in detail. In Section 8 the materials and methods of the field experiments are described. In Section 9 the results of the computer simulations and the field experiments are shown and discussed. Finally, in Section 10 the future development of this research work are discussed.

2. Related works

Since the 1990s, protecting CMIs has become increasingly crucial for both academia and the maritime industry. In this context, surveillance and patrolling operations play a fundamental role. Reviews addressing the use of autonomous marine vehicles for surveillance purposes can be found in Manzari (2020) and Ferri et al. (2017), while cooperative patrolling scenarios involving heterogeneous agents are presented in Birk et al. (2012). However, these works mainly focus on the use of Unmanned Underwater Vehicles (UUVs). More recently, small Maritime Autonomous Surface Ships (MASSs) have been identified as a suitable solution for CMI surveillance (Elkins et al., 2010), especially considering that many attacks rely on surface vessels as operational bases (Kantchev, 2023). Another contribution describing a platform for monitoring large maritime areas can be found in González-Reolid et al. (2018).

Several contributions in the literature therefore address the use of MASSs for surveillance and patrolling applications, often focusing on the Guidance, Navigation, and Control (GNC) modules enabling autonomous operation. The literature proposes a wide variety of GNC architectures, each designed to pursue different objectives and satisfy different operational requirements. Depending on the specific task, these architectures may prioritise accurate path tracking, station-keeping, collision avoidance, or long-term area monitoring, and many have been validated through experimental campaigns and real-world deployments. Several contributions on real-world tests of GNC architectures are available in the literature; examples include the following. In Hinostroza et al. (2025), experimental tests related to track keeping and dynamic positioning are presented compared to a simulated one. In Breivik et al. (2008), a real test of a target tracking scenario is presented. In He et al. (2024) the test of a GNC system tailored for doing collision avoidance in narrow water is presented; while, in the end, in Kim et al. (2024) the test of a GNC architecture for narrow canal regions is tested.

From a system-level perspective, a MASS-based surveillance platform is typically required to integrate multiple tightly coupled tasks, many of which have been extensively investigated in the literature. A key first aspect concerns path planning and area coverage, which are essential to ensuring effective patrolling of the area of interest. Deterministic coverage path planning algorithms are surveyed in Tan et al. (2021), while stochastic approaches based on Markov Chains are reviewed in Duan and Bullo (2021). A hybrid solution combining pseudorandom cell selection with deterministic path execution is proposed in González-Reolid et al. (2018). The problem of collision-free path planning has also been addressed using different optimisation strategies, such as particle swarm optimisation (Zadeh et al., 2022), the A∗ algorithm (Song et al., 2019), and dynamic programming methods (Zaccone, 2024). Once a path is defined, reference generation can be achieved either through path-following or track keeping approaches, as discussed in Fossen (2011).

To execute the planned motion, the autonomous vessel must reliably estimate its state and regulate its behaviour accordingly. It is commonly achieved by filtering GNSS data (Lou et al., 2024) or by integrating GNSS measurements with inertial sensors (Xia and Wang, 2016), as reviewed in Fossen (2011). Based on these estimates, different control strategies can be employed, including path-following controllers (Thyri et al., 2021, Donnarumma et al., 2015), dynamic positioning systems (Sørensen, 2011, de Kruif, 2024), and trajectory-tracking controllers, such as MPC-based solutions (Martinsen et al., 2022). Controllers that explicitly account for collision avoidance are presented in Donnarumma et al. (2020), and experimental validations of various control architectures are reported in Wang et al. (2024) and He et al. (2023).

In addition to motion-related functionalities, environmental perception represents a crucial component of a surveillance system. A wide range of sensors can be employed for this purpose (Thombre et al., 2022), including LiDAR (Ponzini et al., 2025b), radar systems (Ludeno et al., 2023), and optical sensors (Molina-Molina et al., 2021), often combined within sensor-fusion frameworks to improve robustness and detection capabilities (Tarasi et al., 2024, Clunie et al., 2021). Several works demonstrate the integration of such perception systems on autonomous surface platforms, both for obstacle detection in structured environments (Molina-Molina et al., 2021, Zhang et al., 2021) and for surveillance and interception tasks (Simetti et al., 2012).

3. Autonomous surveillance platform architecture

The autonomous surveillance platform described and investigated in this paper follows the one presented in (Ponzini et al., 2024). Figure 1 presents the functional scheme of the proposed architecture in the previous paper. In addition to the guidance, navigation, and control systems, the complete architecture includes a shadow vessel monitoring system dedicated to detecting intruders within the AOI. The object of this paper is the subset of the complete architecture highlighted in blue in Figure 1. This part of the architecture serves as the enabling technology for the entire platform, as it embeds systems for motion control, surveillance path generation, and MASS state estimation. The overall structure is described below, along with brief details on the subsystems not involved in the proposed test and not explained in detail in the following sections of the paper.

The coverage algorithm, implemented in the guidance system, calculates the surveillance path in real-time by generating a target waypoint $\mathbf{WP}_{\text{target}}$ each time the previous target waypoint is reached. $\mathbf{WP}_{\text{target}}$ is generated so that the overall surveillance path is random, to reduce the vulnerability of the platform to attack based on pattern recognition, and based on the occupancy grid provided by the environmental perception subsystem of the navigation system. The collision-free path planner computes a sequence of waypoints $\mathbf{WP}_{\text{list}}$ to reach $\mathbf{WP}_{\text{target}}$ while avoiding obstacles in the AOI. The track keeping algorithm calculates the desired pose $\boldsymbol{\eta}_{TR}$ and speed $\boldsymbol{\nu}_{TR}$ vectors at each time step needed to follow $\mathbf{WP}_{\text{list}}$ with an assigned speed. The coverage and track keeping algorithms are used in the experiments and are described in detail in Section 5. The collision-free path

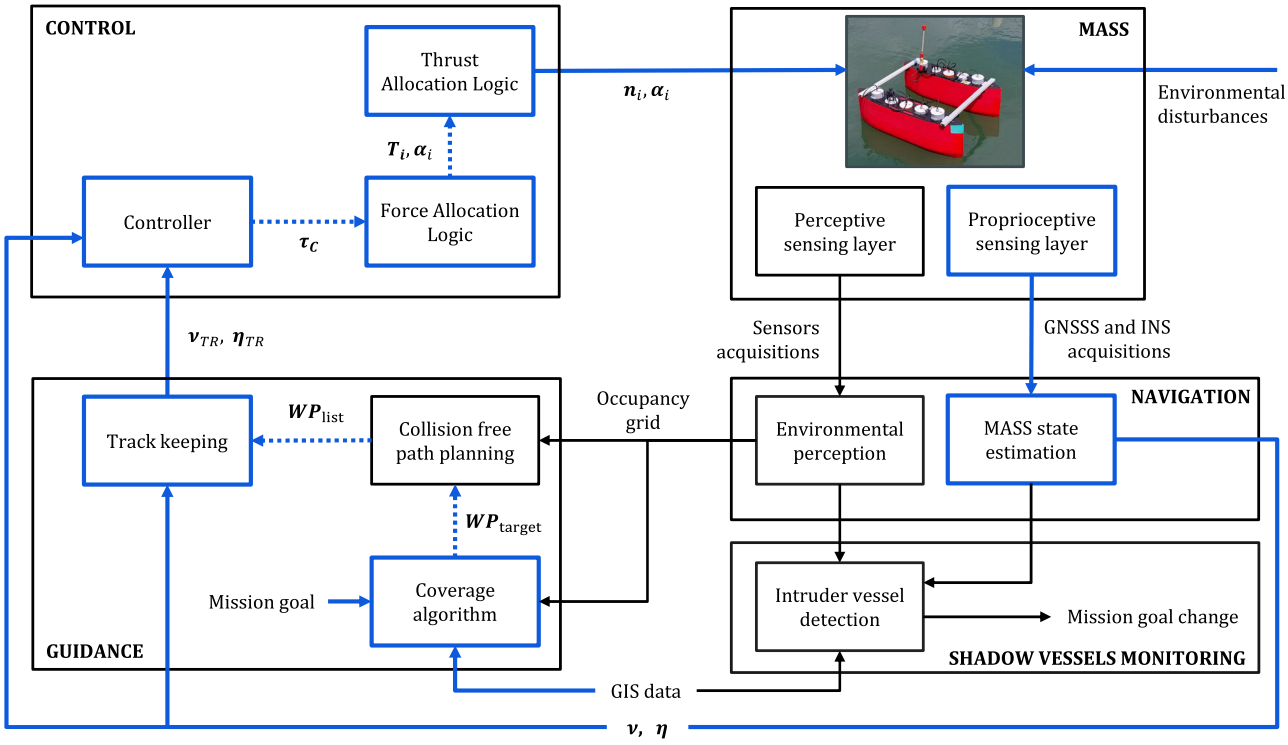

Figure 1. MASS architecture.

planner is not used in the experiments because the designated experimental area contains no obstacles. It is, however, fully described and validated in (Zaccone and Martelli, 2018).

A control system in 3 Degrees Of Freedom (3-DOF), accounting for large drift angles, is adopted in this paper to control the surge, sway and yaw motion of the MASS. This approach, in principle, enables highly precise motion of the MASS, making it suitable for use in complex environments with numerous obstacles. The control system comprises three subsystems: the controller, the Force Allocation Logic (FAL), and the Thrust Allocation Logic (TAL). The controller computes the required force vector $\boldsymbol{\tau}_C$ to drive the error between the desired setpoints and the MASS state estimate to zero. The FAL distributes $\boldsymbol{\tau}_C$ between the actuators of the MASS calculating the thrust vectors each one is required to deliver. These thrust vectors are uniquely identified by their moduli T_i and angles α_i with respect to the MASS bow as shown in Figure 2. The TAL calculates the setpoints for the actuators' internal control systems required to deliver the thrust vectors. A detailed description of the controller, FAL, and TAL is provided in Section 6. The setpoints for the actuators are finally transmitted to the MASS.

In the proposed architecture, the environmental perception and state estimation subsystems are integrated into the navigation system.

The environmental perception subsystem processes data from the perceptive sensing layer to detect objects within the AOI. For this purpose, Ponzini et al. (2024) presents a stand-alone LiDAR sensor with low computational cost that can, in principle, be configured modularly. Meanwhile, the MASS state estimation subsystem utilises inputs from the proprioceptive sensing layer to estimate the generalised pose ($\boldsymbol{\eta}$) and velocity $\dot{\boldsymbol{\eta}}$ vectors. The MASS state estimator is based on the Kalman Filter and is described in detail in Section 7.

The perceptual system for navigation and surveillance tasks can be configured modularly, with the primary aim of detecting intruder vessels. A possible use of a stand-alone LiDAR sensor with low computational impact for performing this task has been proposed

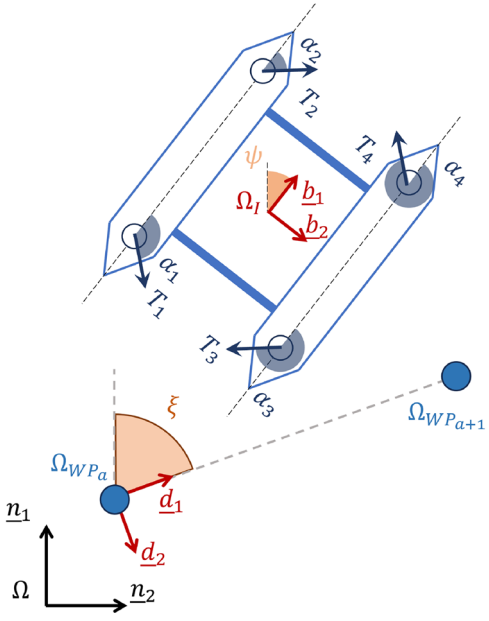

Figure 2. Reference frames.

in Ponzini et al. (2024), where the shadow vessel monitoring system continuously analyses LiDAR point cloud and compares it with Geographic Information System (GIS) data to detect unregistered or unexpected vessels. Such a detection pipeline can be easily extended to include target point cloud classification, as formulated and extensively tested in Ponzini et al. (2025b). Depending on operational needs and on the specific task, the system's modularity allows for the implementation of perceptual modules based on multimodal detection; a suitable decision level fusion framework for LiDAR and RGB images was illustrated and evaluated by Ponzini

and Martelli (2025), while a data-level fusion framework to integrate LiDAR point cloud and thermal imaging was described and tested in Ponzini et al. (2025a). Upon detection of a target intruder vessel, the surveillance mission is deemed complete, and additional logic may be activated depending on the operational scenario, as previously illustrated for target tracking in Fruzzetti et al. (2024a).

4. Reference frames and kinematics

This section introduces the reference frames used in this work and the corresponding transformations between them. It also includes the kinematic formulations associated with these frames. Figure 2 illustrates the coordinate systems that will be referenced throughout the paper:

- The n-frame $\{\mathbf{\Omega}, \underline{n}_i\}$ is the inertial Earth-fixed frame. The origin $\mathbf{\Omega}$ is located on the mean water-free surface at an appropriate location. The positive unit vector $\underline{n}_1$ points towards the North, $\underline{n}_2$ points towards the East, and $\underline{n}_3$ points downwards.
- The b-frame $\{\mathbf{\Omega}_I, \underline{b}_i\}$ is fixed to the vessel hull. The origin, $\mathbf{\Omega}_I = x_I\underline{n}_1 + y_I\underline{n}_2$, is located in the middle of the vessel length taken along the symmetry axes, and on the waterline. The positive unit vector $\underline{b}_1$ points towards the bow, $\underline{b}_2$ points towards starboard, and $\underline{b}_3$ points downwards.
- The d-frame $\{\mathbf{\Omega}_{WP_a}, \underline{d}_i\}$ is fixed with the path defined by the two waypoints selected at each time step ($\mathbf{\Omega}_{WP_a}$ and $\mathbf{\Omega}_{WP_{a+1}}$) by the track keeping guidance. The origin is in $\mathbf{\Omega}_{WP_a} = x_{WP_a}\underline{n}_1 + y_{WP_a}\underline{n}_2$, the positive vector $\underline{d}_1$ points towards the vector $(\mathbf{\Omega}_{WP_{a+1}} - \mathbf{\Omega}_{WP_a})$, $\underline{d}_2$ points towards starboard, and $\underline{d}_3$ points downwards.

The reference systems lie in the same plane and are related by the Euler angle and the relative rotations in (1). The generic rotation matrix is shown in (2).

$$\underline{n} = \boldsymbol{R}^{n}_{\underline{b}}(\psi)\,\underline{b}, \quad \underline{n} = \boldsymbol{R}^{n}_{\underline{d}}(\xi)\,\underline{d} \tag{1}$$

$$\boldsymbol{R}^{n}_{\underline{b}/\underline{d}}(\star) = \begin{bmatrix} \cos\star & -\sin\star & 0 \\ \sin\star & \cos\star & 0 \\ 0 & 0 & 1 \end{bmatrix} \tag{2}$$

where ψ is the heading angle, ξ is the angle defined by the vector $(\mathbf{\Omega}_{WP_2} - \mathbf{\Omega}_{WP_1})$ and $\underline{n}_1$, and $\bigstar$ is the generic angle between the selected reference frames.

The adopted pose $\boldsymbol{\eta} = [x, y, \psi]$ and speed $\boldsymbol{\nu} = [u, v, r]$ arrays in this paper are, respectively, the positions with respect to the origin of the $\underline{n}$ frame and the heading angle, and the speed components in the $\underline{b}$ frame. Moreover, the speed array in the $\underline{n}$ frame is $\dot{\boldsymbol{\eta}} = [V_x, V_y, r]$.

5. Guidance system

This section describes in detail the coverage algorithm and the track keeping subsystem of the guidance system, which are the parts validated in the field experiments.

5.1. Coverage algorithm

The coverage subsystem is the core of the proposed guidance strategy. It implements a stochastic coverage algorithm with a twofold objective: to ensure full coverage of the AOI and to generate a random surveillance path. The first objective ensures that no parts of the AOI are left unsurveilled by the MASS; the minimises the vulnerability to exploits based on pattern recognition. It is to be noticed that no constraints are imposed on the coverage speed, as it can always be achieved by increasing the MASS speed without modifying the coverage algorithm.

To satisfy the requirements stated in the previous paragraph, a stochastic coverage algorithm based on that proposed by Duan and Bullo (2021) is designed. The stochastic coverage algorithm proceeds as follows:

Algorithm 5.1: Stochastic Coverage Algorithm

Step 1: Partition the AOI into square cells of side equal to l;
Step 2: Randomly select a cell which is at least at $d_{\text{proximity}}$ from the MASS' current position and return its centroids as $\mathbf{WP}_{\text{target}}$;
Step 3: When $\mathbf{WP}_{\text{target}}$ is reached go to *Step* 2.

The parameter l is to be chosen relatively to the MASS dimensions. The parameter $d_{\text{proximity}}$ is to be chosen so that the track between the MASS's current position and $\mathbf{WP}_{\text{target}}$ is long enough to allow proper acceleration and deceleration phases as required by track keeping guidance from Section 5.2.

Algorithm 5.1 realises a Markov Chain in which the states coincide with the centroids of the cells of the partitioned AOI. This guarantees that the surveillance path is random, satisfying one of the two design criteria. The full coverage of the AOI is guaranteed only in case that the Markov Chain realised by Algorithm 5.1 is irreducible, which means that there must always exist a path between any pair of states in the Markov Chain state graph. A sufficient condition for this can be derived as a condition on the value of $d_{\text{proximity}}$.

Let P indicate the partitioned AOI as a set of locations on the Euclidean plane. Based on how the stochastic coverage algorithm is defined, for every pair of locations $\mathbf{p}, \mathbf{q} \in P$, $\mathbf{q}$ is reachable from $\mathbf{p}$ if $d(\mathbf{p}, \mathbf{q}) \geq d_{\text{proximity}}$, where $d(\star, \star)$ is the euclidean distance, or if there is a third location $\mathbf{s}$ such that $d(\mathbf{p}, \mathbf{s}) \geq d_{\text{proximity}}$ and $d(\mathbf{s}, \mathbf{q}) \geq d_{\text{proximity}}$. Let $d_{\text{min,max}}$ indicate the minimum of the maximum distances between any pair of locations in $P_{\text{partition}}$. $d_{\text{min,max}}$ can be calculated as below:

$$d_{\text{min,max}} = \min_{\mathbf{p}} \max_{\mathbf{s}} d(\mathbf{p}, \mathbf{s}) \tag{3}$$

By the definition of $d_{\text{min,max}}$, for every location $\mathbf{p}$ it is guaranteed the existence of another location $\mathbf{s}$ such that $d(\mathbf{p}, \mathbf{s}) \geq d_{\text{min,max}}$. From the triangular inequality and from the fact that $d(\mathbf{p}, \mathbf{s}) \geq d_{\text{min,max}}$ and $d(\mathbf{p}, \mathbf{q}) \geq d_{\text{proximity}}$ it is possible to derive the following property of $\mathbf{s}$ and $\mathbf{q}$:

$$d(\mathbf{s}, \mathbf{q}) \geq d_{\text{min,max}} - d_{\text{proximity}} \tag{4}$$

The value of $d_{\text{min,max}}$ is a property of P which is difficult to control, while $d_{\text{proximity}}$ is an arbitrary parameter, therefore it is possible to choose it such that $d_{\text{min,max}} - d_{\text{proximity}} \geq d_{\text{proximity}}$, therefore making $\mathbf{q}$ reachable from $\mathbf{s}$. The choice of $d_{\text{proximity}}$ must satisfy the following condition:

$$d_{\text{proximity}} \leq d_{\text{min,max}}/2 \tag{5}$$

It is worth pointing out that Equation (5) is not a necessary and sufficient condition for the full coverage of the AOI since the irreducibility of the Markov Chain realised by the coverage algorithm can be satisfied by conditions other than only those presented above, but it is sufficient to ensure the full coverage of the AOI.

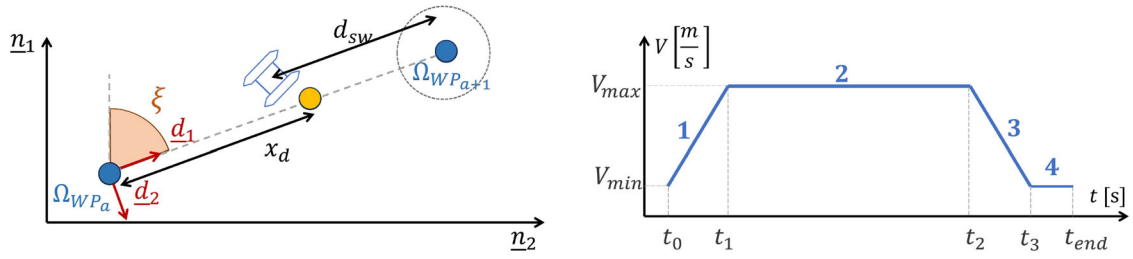

(a) Layout. (b) Speed Law.

Figure 3. Track Keeping motion control scenario. (a) Layout. (b) Speed Law.

5.2. Track keeping subsystem

A track keeping algorithm is used to generate the setpoints necessary to follow the surveillance path with a prescribed speed. The reference implementation of the track keeping algorithm is described in Fruzzetti et al. (2024b). The selected track keeping algorithm adopts a trapezoidal velocity profile, and it was selected to ensure generalizability to more complex maritime areas, where a combination of fixed and dynamic obstacles requires high precision near the waypoints. The inputs are the waypoints list $\mathbf{WP}_{\text{list}}$ and the pose feedback $\boldsymbol{\eta}$. At the same time, the outputs are the time history of the trajectory $\boldsymbol{\eta}_{TR}$ and the desired velocity $\boldsymbol{\nu}_{TR}$.

At each time step, two consecutive waypoints are selected from the waypoint list $\mathbf{WP}_{\text{list}}$ given as input, leading to the definition of the $\underline{d}$ reference frame described in Section 4. At the initial instant, the first waypoint $\mathbf{WP}_1$ is taken as the initial position of the vessel at the moment at which the architecture is started. The resulting draft is shown in Figure 3(a), which shows the resulting draft and outlines the angle ξ between the positive unit vector $\underline{n}_1$ of the inertial frame and $\underline{d}_1$. The switch at the following waypoints couple occurs when the along-track distance with respect to $\boldsymbol{\Omega}_{WP_2}$, d_{sw}, is lower than a given distance nL_{PP}.

The speed setpoint $V(t)$ is defined according to the trapezium speed law shown in Figure 3(b) between each couple of waypoints. Four phases are identified in this law, including deceleration, acceleration, and constant speed phases between the selected maximum speed V_{max} and the selected minimum speed V_{min}. The durations of the acceleration and deceleration phases are determined by the user-defined maximum acceleration. The desired speed array trajectory results in (6).

$$\boldsymbol{\nu}_{TR} = [V(t) \quad 0 \quad 0]^T \tag{6}$$

The desired instantaneous position $\boldsymbol{x}_d(t)$, the yellow point in Figure 3(a), is defined following the kinematics outlined by the trapezium speed profile in the $\underline{d}$ frame and then rotated in $\underline{n}$ to obtain the desired position trajectory $\boldsymbol{\eta}_D^*$ as shown in (7). To compute the heading missing setpoint, two contributions are taken into account: the geometric angle $\xi(t)$, which depends on the orientation defined by the active waypoint pair, and the Line-Of-Sight correction term ψ_{LOS} (8) according to Fruzzetti et al. (2024a), applied to compensate for the cross-track error along $e_{\underline{d}_2}$. Both contributions are ultimately provided gradually through a ramp between the times t_0 and t_1 defined as in Figure 3(b), establishing a smooth heading setpoint $\phi(t)$ at each time step. This strategy prevents abrupt variations in the commanded angle when switching from one waypoint pair to the next.

$$\boldsymbol{\eta}_D^* = \boldsymbol{R}(\xi(t))[x_d(t) \quad 0 \quad 0]^T + \boldsymbol{\Omega}_{WP_1} \tag{7}$$

$$\psi_{LOS} = \arctan \frac{e_{\underline{d}_2}}{\Delta} \tag{8}$$

$$\boldsymbol{\eta}_{TR} = [\boldsymbol{\eta}_D^*(1:2) \quad \phi(t)]^T \tag{9}$$

where Δ is the distance by which it is supposed to come back to the desired leg.

6. Control system

This section describes in detail all subsystems of the control system, which are validated through simulation and field experiments.

6.1. Controller

A 3-DOF controller is adopted to control all three planar motions: surge, sway, and yaw. The controller calculates the forces and moment vector $\boldsymbol{\tau}_C$ necessary to nullify the error between the desired ($\boldsymbol{\eta}_{TR}$, $\boldsymbol{\nu}_{TR}$) and feedback ($\boldsymbol{\eta}$, $\boldsymbol{\nu}$) pose and speed. The controller selected for the final version is a PID controller with an antiwindup system, as in (10), according to Martelli et al. (2020).

$$\begin{aligned}\boldsymbol{\tau}_C = {} & K_P(\mathbf{R}^T(\psi)(\boldsymbol{\eta}_{TR} - \boldsymbol{\eta})) + K_D(\boldsymbol{\nu}_{TR} - \boldsymbol{\nu}) \\ & + K_I \int (\mathbf{R}^T(\psi)(\boldsymbol{\eta}_{TR} - \boldsymbol{\eta}) - K_{aw}(\boldsymbol{\tau}_C - \boldsymbol{\tau}))\, \mathrm{d}t\end{aligned} \tag{10}$$

where $\mathbf{K}_P$, $\mathbf{K}_I$, $\mathbf{K}_{aw}$ and $\mathbf{K}_D$ are positive diagonal matrices containing the proportional, integral, antiwindup, and derivative gains, respectively and $\boldsymbol{\tau}$ is the forces and moment vector actually actuated.

6.2. Force allocation logic

The FAL calculates the thrust that each actuator needs to push. For the experimental validation, the SWAMP-class MASS that is described in Section 8 is adopted. It is equipped with four pump-jets placed at the bow and stern of the hulls as shown in Figure 2. For each pump-jet, it is necessary to determine the thrust modulus T_i and the angle with respect to the bow α_i, and the thrusts summed up must equate $\boldsymbol{\tau}_C$. This leads to an allocation problem with 3 equations (the equilibrium in the horizontal plane) and 8 unknowns.

Several techniques have been proposed in the literature; examples can be found in De Wit (2009) and Johansen and Fossen (2013) for solving the allocation problem. In this application, the number of unknowns is reduced, fixing the direction of the pump-jets α_i to $[135°, 45°, -135°, -45°]$ as shown in Figure 2. This choice of the angles α_i allows for an increase in the robustness of the propulsion system, although it reduces the maximum yaw moment deliverable. To determine T_i an optimisation problem in (11) where the aim is to minimise the sum of the moduli of the thrusts while ensuring the equilibrium of the horizontal plane forces and moment given by the pump-jets, $\boldsymbol{\tau}_{AZ_i}$, with $\boldsymbol{\tau}_C$ and respecting the minimum and the maximum available thrusts. The optimal allocation problem is solved

using quadratic programming techniques in real time.

$$\begin{aligned} \underset{T_1,\ldots,T_4}{\text{minimize}} \quad & \sum_{i=1}^{4} \frac{T_i^2}{T_{\max}^2} \\ \text{subject to} \quad & \sum_{i=1}^{4} \boldsymbol{\tau}_{AZ_i} = \boldsymbol{\tau}_C \\ & T_{\min} \leq T_i \leq T_{\max}, \quad i = 1, \ldots, 4 \end{aligned} \tag{11}$$

where $\boldsymbol{\tau}_{AZ_i}$ is the ith thrust vector with modulus T_i and angle with respect to the bow α_i.

6.3. Thrust allocation logic

The TAL calculates the control signals for the actuators of the MASS to make them deliver the thrusts calculated by the FAL. Because SWAMP has four pump-jets as actuators, to control them it is required to calculate the orientation angles of the nozzles with respect to the bows δ_i and the revolution speed of the impellers n_i. The values of δ_i coincide exactly with the angle α_i while the values for n_i are calculated from T_i based on combinatorics curves.

7. Navigation system

This section describes in detail the MASS state estimation procedure of the navigation system, which is validated in the field experiments.

Accurate vessel state estimation is essential for guidance and control systems, enabling the MASS to perform its tasks effectively. To achieve this, the navigation system must integrate a robust sensing layer that processes data to extract meaningful information and construct the state vector by measuring and estimating the necessary parameters. The vessel state estimation primarily relies on data gathered by onboard sensors and a standard Kalman Filter (KF) (Maybeck, 1990), utilising a fully kinematic, constant-velocity state transition model.

The sensors considered to be onboard the MASS are a GNSS receiver and an INS. The GNSS receiver provides latitude and longitude, while the INS, through its embedded gyro and magnetometer, supplies the heading angle ψ and the rate of turn r. To integrate GNSS data into the navigation system, the latitude and longitude coordinates $(lat_{\boldsymbol{p}}, lon_{\boldsymbol{p}})$ are first converted into Universal Transverse Mercator (UTM) coordinates (Snyder, 1987), using local Easting and Northing references. The GNSS position is then expressed in the inertial frame $(\underline{n})$, which is defined at a reference location $\boldsymbol{\Omega}$ with known coordinates $(lat_{\boldsymbol{\Omega}}, lon_{\boldsymbol{\Omega}})$, following the transformation in (12). Under these conditions, the KF measurement vector becomes $\boldsymbol{z} = [x, y, \psi, r]$. The use of the KF not only stabilises the measured quantities but also enables the estimation of unmeasured variables, i.e. V_x and V_y.

$$\boldsymbol{z}(1:2) = \boldsymbol{\zeta}(lat_{\boldsymbol{P}}, lon_{\boldsymbol{P}},) - \boldsymbol{\zeta}(lat_{\boldsymbol{\Omega}}, lon_{\boldsymbol{\Omega}}) \tag{12}$$

where $\boldsymbol{\zeta}$ refers to the UTM conversion function.

8. Material and methods

This section outlines the software and the hardware setup used for the field experiments, with details on sensors, sensors' mounting on the test vehicle and general hardware. In addition, the indicator selected for evaluating the proposed system is discussed.

8.1. Hardware

The Shallow Water Autonomous Multipurpose Platform (SWAMP) (Odetti et al., 2020), a fully electric catamaran, is selected as a case study. It is equipped with an embedded Inertial Navigation System (INS), Global Navigation Satellite System (GNSS) receivers, and it is designed to accommodate a LiDAR unit and optical sensors (operating in both the visible and infrared spectrum), which form the sensing layers of the system. Communication between components and the shore control centre is ensured by Wi-Fi connection. To obtain the vessel's position and orientation data, a Xsens MTi-G-710 GNSS/INS system is employed, whose technical specifications are provided in Table 1. The SWAMP-class vehicle equipped with the sensor suite in the field test environment is shown in Figure 4(a), while the schematic representation of the vehicle with the sensor's mounting points is shown in Figure 4(b). From the layout, it is evident that the GNSS receiver is positioned approximately amidships, while the INS is mounted 350 mm above.

Table 1. GNSS/INS technical specifications.

Sensor	Spec.	Value
Gyroscope	Standard full range	450 deg/s
	In-run bias stability	10 deg/h
	Noise density	0.01 °/s/$\sqrt{Hz}$
Accelerometer	Standard full range	20 g
	In-run bias stability	15 μg
	Noise density	0.01 °/s/$\sqrt{Hz}$
Magnetometer	Standard full range	+/− 8 G
	Total RMS Noise	0.5 mG
	Resolution	0.25 mG
GNSS receiver	Brand	u-blox
	Model	MAX-M8
	Accuracy	1 m

The sensor suite is connected to an onboard processing unit, specifically a semi-rugged PC housed on the vessel deck, and further protected by a soft dry bag, whose specifications are given in Table 2.

The onboard computational module is in charge of reading the sensor data, performing data parsing and primary processing, and publishing the resulting data to the communication layer. The processed data are published on specific topics using the MQTT (Message Queuing Telemetry Transport) protocol, exploiting a Wi-Fi network created by an access point located on board the vessel. On the shore resides a second computational module that is subscribed to the topics and has the ability to log data or perform additional processing. In this architecture, the on-board or shore process units are nodes and additional nodes can be inserted for any need. On the same network, control commands are sent to the propulsion modules. Each propulsion module constitutes a separate node, and each hull is managed by Raspberry Pi 3.0 model B SBC (Single Board Computer) running the Raspbian OS (Operating System). For additional details on the vessel's architecture, please refer to the original paper (Odetti et al., 2020).

8.2. Test procedures and indicators

The GNC system of the surveillance platform presented in the previous sections of this paper is validated with both a numerical simulation and a field experiment.

The numerical simulation consists of a simulated surveillance operation in which a simplified mathematical model of SWAMP is required to surveil a virtual AOI whose boundaries coincide with those of the environment in which the field experiment takes place. The objective of the numerical simulation is twofold: first, to provide preliminary validation of the guidance and control systems; and second, to demonstrate the ability of the coverage to encompass the entire AOI.

The field experiment consists of a surveillance operation taking place in an artificial lake located in the province of Piacenza, Italy,

(a) Swamp-class vehicle in test field.

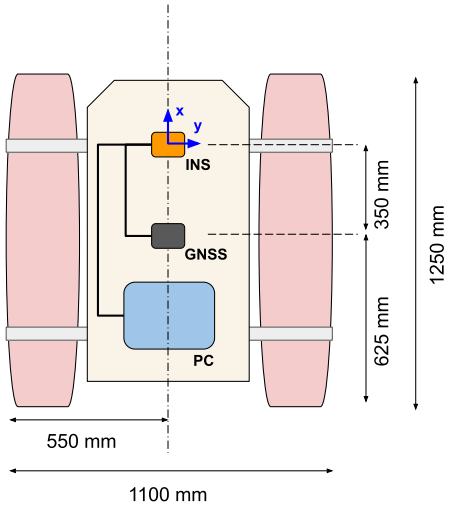

(b) Sensors layout.

Figure 4. SWAMP-class vehicle outfitted for the field test campaign. (a) Swamp-class vehicle in test field. (b) Sensors layout.

Table 2. Onboard computer main specifications.

Spec.	Value
OS	Fedora Linux 41
Kernel	6.13.10
CPU	Intel Core i3-1115G4 4.10 GHz
RAM	8GB DDR4

Table 3. Input parameters for the patrolling simulation.

l [m]	margin [m]	$\mathbf{d}_{proximity}$ [m]
2	3	10

at 44.92682°N 9.57081°E and shown in Figure 5(a). This lake has a maximum spacing of approximately 100 x 60 m, however, it is big enough to grant SWAMP freedom of movement, but small enough so that it is entirely covered by the Wi-Fi network, thus communication between the shore station and SWAMP is never lost. The objective of the field experiment is to validate the integration of the guidance, navigation, and control systems and demonstrate the robustness of the GNC system.

The AOI to be surveyed is a polygon representing a portion of the entire lake for both the experimental and simulation campaigns. The boundary of the AOI and its partition are shown in Figure 5(b), Table 3 shows the parameters for the coverage algorithm. Because SWAMP is not equipped with a perceptive sensor in both the simulation and the field experiment, the value of l is chosen so that each cell is approximately the same size as SWAMP. The value of $d_{\text{proximity}}$ is

(a) Aerial View.

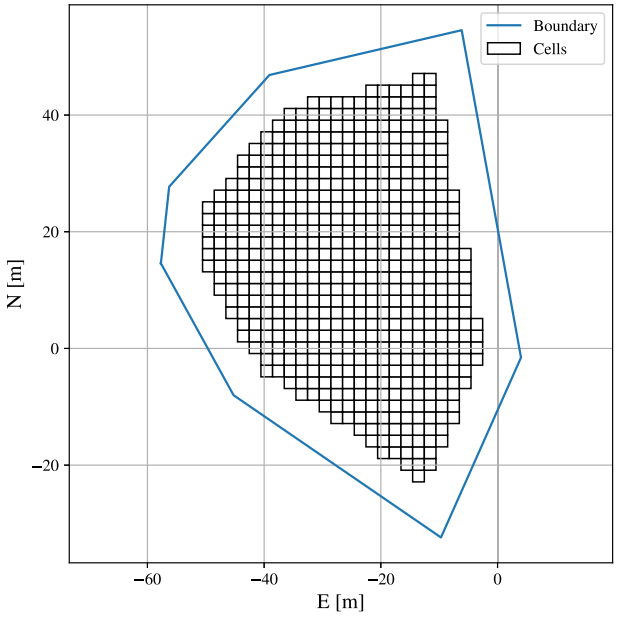

(b) Cells of the partitioned AOI.

Figure 5. Test site. (a) Aerial View. (b) Cells of the partitioned AOI.

chosen to ensure the legs have a minimum length compatible with the velocity profile adopted in the track keeping algorithm. The 'margin' is introduced to create a buffer zone from the boundary of the AOI, allowing SWAMP to manoeuvre freely and to account for possible seasonal variations in the lake boundaries.

The results of the numerical simulation and field experiment are analysed and discussed following both a quantitative approach based on a set of Key Performance Indicators (KPIs) defined to describe the performance of the GNC system. These metrics are the Mean Cross-Track Error (*MCTE*), the Maximum Cross-Track Error (*MaCTE*), the Mean Along-Track Error (*MATE*), the Mean Path-Tangential Angle Error (*MPTE*), the Mean Speed Over Ground Error (*MSOGE*), and the Mean Rate Of Turn Error (*MROTE*).

The *MCTE* is the mean value of the transversal deviation $e_{\underline{d}_2}(t)$ of SWAMP with respect to the surveillance path. This KPI is considered the primary measure of respect for the other, given the intended objectives of the proposed system. For a single leg $e_{\underline{d}_2}(t)$ can be calculated as in (13), while the *MCTE* can be calculated as in (14).

$$e_{\underline{d}_2}(t) = |\mathbf{R}(\xi)(\boldsymbol{\eta}(t) - \boldsymbol{\eta}_{TR}(t)) \cdot \underline{\mathbf{d}}_2| \tag{13}$$

$$MCTE = \frac{1}{t_e - t_0} \int_{t_0}^{t_e} e_{\underline{d}_2}(t)\, \mathrm{d}t \tag{14}$$

where t_0 and t_e denote the start and end times of the entire time series analysed.

The *MaCTE* is the maximum value of the transversal deviation $e_{\underline{d}_2}(t)$ of SWAMP with respect to the surveillance path.

The *MATE* is the mean value of the longitudinal deviation $e_{\underline{d}_1}(t)$ of SWAMP with respect to the surveillance path. For a single leg $e_{\underline{d}_1}(t)$ can be calculated as in (15), while the *MATE* can be calculated as in (16).

$$e_{\underline{d}_1}(t) = |\mathbf{R}(\xi)(\boldsymbol{\eta}(t) - \boldsymbol{\eta}_{TR}(t)) \cdot \mathbf{d}_1| \tag{15}$$

$$MATE = \frac{1}{t_e - t_0} \int_{t_0}^{t_e} e_{\underline{d}_1}(t)\, \mathrm{d}t \tag{16}$$

The *MPTE* is the mean value of the deviation of SWAMP's heading with respect to the heading required by the trajectory $\psi_{TR}(t)$. The *MPTE* is calculated as in (17).

$$MPTE = \frac{1}{t_e - t_0} \int_{t_0}^{t_e} |\psi(t) - \psi_{TR}(t)|\, \mathrm{d}t \tag{17}$$

The *MSOGE* is the mean of the error between SWAMP's Speed Over Ground (SOG) and the SOG prescribed by the trajectory $V_{TR}(t)$. The *MSOGE* is calculated as in (18).

$$MSOGE = \frac{1}{t_e - t_0} \int_{t_0}^{t_e} |V(t) - V_{TR}(t)|\, \mathrm{d}t \tag{18}$$

where $V(t) = \sqrt{u(t)^2 + v(t)^2}$.

The *MROTE* is the mean of the error between SWAMP's Rate Of Turn (ROT) and the ROT prescribed by the trajectory $r_{TR}(t)$. The *MROTE* is calculated as in (19).

$$MROTE = \frac{1}{t_e - t_0} \int_{t_0}^{t_e} |r(t) - r_{TR}(t)|\, \mathrm{d}t \tag{19}$$

Alongside the quantitative analysis, a qualitative analysis is also carried out to enrich the results. To this end, the following information is provided: the state estimation system performances, the share of covered AOI as a function of time, the coverage heatmap, and statistical quantities of the surveillance path. The aim of the qualitative analysis is to validate the effectiveness of the state estimation system and the coverage algorithm.

The state estimation system performance is assessed in three dedicated analyses: (i) Compliance with the specified 10 Hz feedback publication frequency is assessed by evaluating timestep accuracy through the mean, median, and standard deviation of the intervals between consecutive samples; (ii) The statistical properties of the KF residuals are analysed. The k^{th} iteration residual is defined as the difference between the predicted state vector projected in the measure space and the measure vector itself. This enables evaluation of whether the KF appropriately tracks the object's true dynamics with respect to the measured quantities. It is used to assess the state estimation system's capability. In addition, the distribution of residuals is checked for normality; (iii) A focused analysis is performed on the quantities that are estimated (and not directly measured) by the system, specifically the velocity components V_x and V_y. In a trajectory leg characterised by pure surge constant speed, the velocities estimated by the filter are compared to those computed via finite differences of position data. The KPI is expressed in terms of the Root Mean Square Error (RMSE) relative to a reference average velocity. It is used to assess the state estimation system's capability.

The effectiveness of the coverage algorithm is assessed by presenting statistical metrics of the generated surveillance path, a heatmap showing AOI coverage, and a graph showing the share of AOI covered over time. The statistical quantities indicate the randomness of the path; the heatmap indicates possible bias in the coverage algorithm; and the share of AOI covered over time provides an estimate of the coverage speed.

9. Results

This section reports the results obtained to validate the proper functioning of the architecture and the integrability of its components. Due to the complexity of the global system, which requires integrating several subsystems to achieve the surveillance objective, multiple development steps must be undertaken to achieve the ultimate goal. An overview of the steps to be carried out to achieve the ultimate goal is described in depth in Section 3 and is presented in Ponzini et al. (2024). Here, all preliminary steps, including the computer simulation phase and testing of the individual components in a virtual scenario, have been presented, demonstrating the functionality of the subsystems and their integration into several preliminary subsets. The results include the coverage performance of the selected area, as provided by the coverage algorithm; the generation of collision-free paths by the path planner; the environment perception capabilities of the perception subsystem; and the intruder detection mechanism within the shadow vessel monitoring system, applied to the critical infrastructure of the Lillgrund Wind Farm. Moreover, physical MASS testing was conducted in a controlled indoor environment using the indoor test tank facility, where the MASS platform's estimation and control capabilities were evaluated. Specifically, the vessel performed autonomous navigation along a sequence of waypoints, thereby testing the Indoor Positioning System's state estimation, control, and track keeping capabilities. The results demonstrated the reliability of the onboard state estimation subsystem and confirmed the feasibility of transferring these functionalities to an outdoor environment.

Verification of the architecture proposed in this paper, shown in blue in Figure 1, is the enabling technology for the entire infrastructure; hence, it is a fundamental step to be achieved, following the steps previously outlined in Ponzini et al. (2024). The results presented here demonstrate the validation and verification of these enabling technologies in a simulated environment and subsequently in a relevant environment.

9.1. Simulation tests

The simulated tests are conducted using a mathematical model that approximates SWAMP dynamics. The model is identified following the procedure proposed in Yasutomi and Fukushima (2015) and Hinostroza et al. (2025), using the experimental data collected during several experimental campaigns conducted with the MASS. This model plays a fundamental role in the subsequent simulation stages, as it provides a reliable representation of system behaviour and enables a realistic evaluation of the proposed strategies.

Both the coverage algorithm's effectiveness in the area and the overall system's effectiveness are evaluated in this phase. The coverage subsystem is implemented in a separate process from the remainder of the system and communicates via MQTT.

The surveillance simulation uses 1000 waypoints generated by the coverage algorithm and simulates patrolling of the AOI for approximately 16 hours. This long-duration simulation allows the evaluation of the proposed framework under realistic operational conditions. The results obtained demonstrate the framework's effectiveness in ensuring persistent area coverage and its robustness against the stochastic variability introduced by the generated paths.

The KPIs presented in Section 8.2 expressing the performance of the tracking system are reported in Table 5, the heatmap is reported in Figure 6(a), and the share of covered AOI in time in Figure 6(b). Moreover, Table 4 shows the mean values and the standard deviation of the leg length and course angle variation between consecutive legs of the surveillance path.

To enhance the reader's understanding, the results are supplemented with time histories for the first 1200 seconds and for 22 waypoints of the entities involved in computing the KPIs. The cross-track, along-track, and angle errors time histories are reported in Figure 6(c), respectively, in red, blue, and light blue. The SOG error and the rotation error are reported in Figure 6(d), respectively in blue and red. In Figure 6(e), the path is shown at the end; the waypoints are numbered and marked with red stars, and the dashed line indicates the resulting desired path. The blue line represents the resulting path of SWAMP and can be coupled with the catamaran shapes to provide information about the heading. The green and red markers represent the initial and final points, respectively.

The data presented in Table 4 show that more than half of the time, the leg length is between 15.68 m and 37.97 m, and the course change is between 74.91° and 172.6°, making it very difficult to predict the position of the waypoints generated.

The heatmap in Figure 6(a) shows that the surveillance path covers the entire AOI but appears to be biased toward the centre of the domain. This bias was expected and is likely due to the mean leg length, which is high relative to the overall dimensions of the AOI, thereby forcing the MASS to almost always pass through the centre of the domain.

Figure 6(b) shows that the surveillance path has an exponential rate of coverage, and more than half of the AOI is covered in the first percentage of time. It is important to note that, during the surveillance simulation, no hypotheses were made about the nature of the perceptive sensor mounted on SWAMP. Therefore, a cell is considered covered only when SWAMPS physically occupies it. In a real-world scenario in which a sensor with a range several times larger than SWAMP's length is employed, the rate of convergence is expected to be faster than that achieved in the surveillance simulation.

Beginning with the analysis of pose-related errors, the magnitudes of the cross-track error metrics MCTE and MaCTE can first be evaluated. The results indicate that MCTE is close to zero, which is fundamental to the objectives of the proposed system, as discussed earlier. To better understand the origin of the MaCTE value, it is necessary to analyse the extract from the time history of the cross-track error e_{d_2} reported in Figure 6(c). It can be observed that, at each change in the waypoint pair, the cross-track error exhibits a peak corresponding to the change in direction, followed by a rapid decay. This behaviour represents a transient response and originates from the physical limitations of the adopted MASS, particularly in terms of available control moment. The maximum value is approximately 2 meters, which coincides with the threshold for switching to the next waypoint pair.

A similar interpretation applies to the along-track error and the resulting MATE metric. In this case, after each transition between waypoint pairs, an error that subsequently decreases is generated. However, unlike the cross-track error, the along-track error does not converge to zero. This behaviour is a direct consequence of the waypoint-switching logic, which is triggered when the distance to the nearest waypoint exceeds 2 m. This value must therefore be explicitly accounted for when evaluating the MATE metric.

Analogous considerations can also be drawn for the MPTE metric and for the heading error e_ψ time histories, which exhibit similar transient behaviours at each waypoint transition and rapidly decay once the vehicle re-aligns with the desired trajectory.

Analogous considerations apply to the velocity-related errors, which remain very limited in terms of MSOGE, whereas larger values are observed for MROTE. The latter exhibits distinct peaks corresponding to waypoint transitions, consistently with the transient dynamics discussed earlier.

9.2. Field experiments

Finally, the results of the outdoor experiment, which integrated the control system, guidance functionalities (coverage and track keeping), the MASS navigation state estimation system, and the physical MASS, are reported here.

The first part of the tests aims to verify the feedback estimation system in the selected fields, adopting the KPI described in Section 8.2. The first KPI reported concerns the verification of timestep consistency. Log files were analysed, which contained the Unix timestamps of each message sent by the state estimation subsystem during a two-day experimental campaign at the selected test site. The average timestep obtained from this analysis was 0.100067 s, with a standard deviation of 0.00028 s, confirming both the system's ability to operate at the desired frequency of 10 Hz and its capability to achieve more than sufficient stability of the signal frequency.

Using the state estimation data relative to the path shown in Figure 8(d), the residuals were evaluated for each iteration. In particular, Table 6 summarises the major statistics of interest. The residual value is generally close to zero. Furthermore, to assess the normality of the residuals, histograms illustrating the residual distribution for each measured variable (see Figure 7(a)) are provided, along with the corresponding Q–Q plot (see Figure 7(b)).

Finally, an analysis was conducted on the quantities estimated but not directly measured by the filter, specifically the two velocities V_x and V_y. Specifically, a pure surge motion test was performed in remote-control mode by sending a constant-velocity command to the vehicle. A reference leg was extracted after the acceleration phase, and both the velocities estimated by the filter and those computed through direct differentiation of position were considered. The velocity signals were then compared against the reference average speed of the leg; statistics of the comparison are reported in Table 7. In conclusion, the Kalman-filter–based feedback system can effectively estimate velocities while simultaneously smoothing measured quantities, ensuring normality of the residuals and reliability relative to the measured values.

The second part of the results, instead, focuses on the real-time experiment of the selected framework. The results indicate a scenario

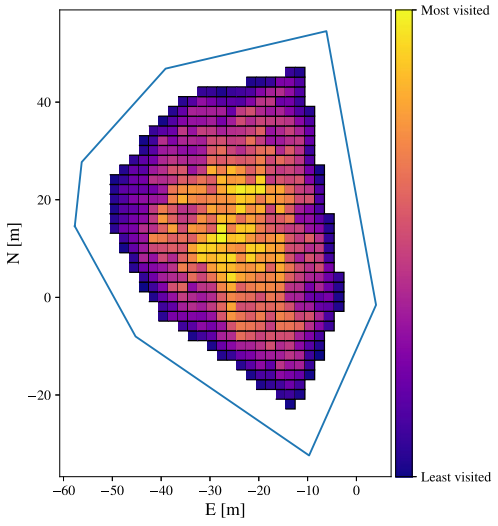

(a) Heatmap.

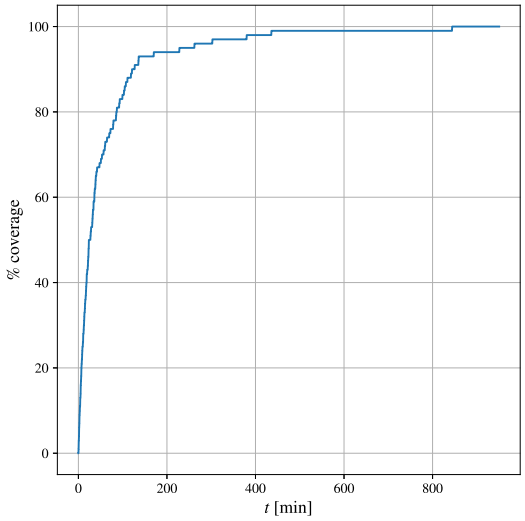

(b) Covered AOI in time.

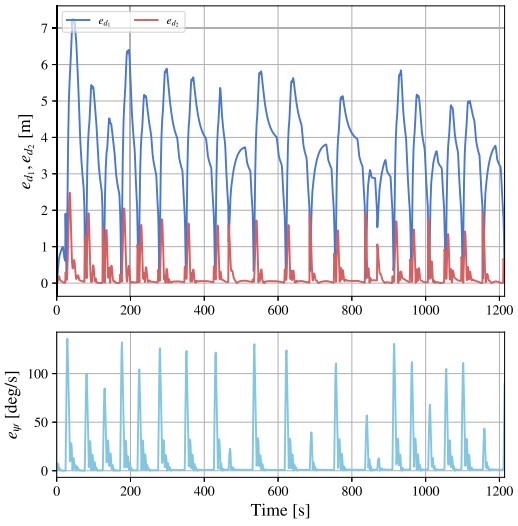

(c) Pose errors.

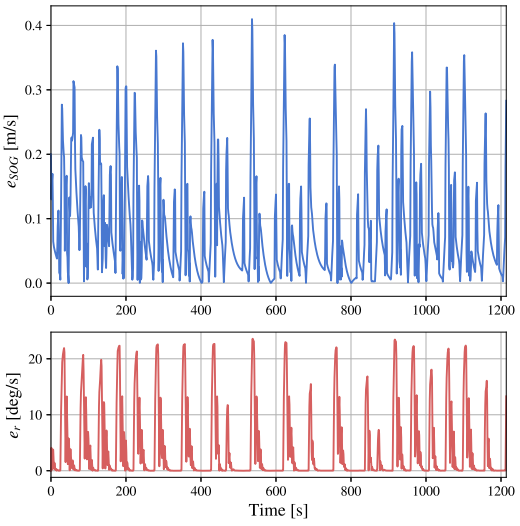

(d) Speed errors.

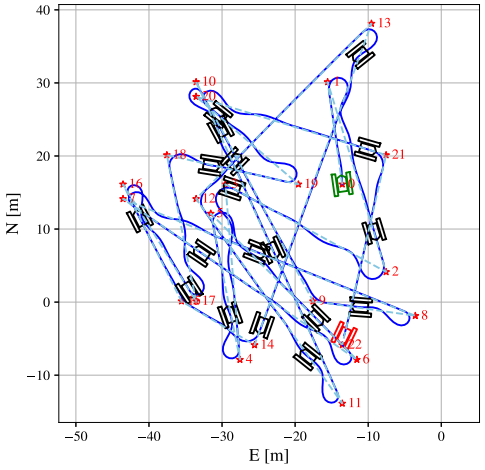

(e) Path.

Figure 6. Simulation results. (a) Heatmap. (b) Covered AOI in time. (c) Pose errors. (d) Speed errors and (e) Path.

Table 4. Statistical parameters of the generated path in the surveillance simulation.

Stat.	leg length [m]	course change [°]
Mean	27.33	123.8
Median	28.28	140.5
σ	11.64	48.88

Table 5. Simulation Results – GNC performance.

MCTE [*m*]	*MaCTE* [*m*]	*MATE* [*m*]	*MPTE* [*deg*]	*MSOGE* [*m*/*s*]	*MROTE* [*deg*/*s*]
0.23	2.48	3.4	11.7	0.08	3.7

Table 6. Statistical KPI indicators of residuals for the estimated states.

Stat.	*x*[*m*]	*y*[*m*]	ψ[*deg*]	*r*[*dps*]
Mean	0.00019	−0.00015	−0.01392	0.02079
σ	0.03752	0.02960	0.37001	1.78554

with 27 waypoints and a duration exceeding 21 minutes. The path covered is shown in Figure 8(d), following the same representation adopted in the previous subsection. The same consideration can be done for the cross-track, along-track, and angle errors time histories reported in Figure 8(e), and for the SOG error and the rate of turn error reported in Figure 8(f). The KPIs related to the tracking performances are reported in Table 8. To complete the results and assess the effectiveness of the coverage, Table 9 shows the statistical quantities of the path, Figure 8(a) reports the heatmap deriving from the experimental test, and Figure 8(c) shows the share of AOI covered over time. To enhance the assessment of coverage, the information is compared with results obtained simultaneously from simulation, hence the heatmap in Figure 8(b).

First, a general qualitative comment on the experimental results can be drawn from the analysis of the overall results and, in particular, the trajectory. As shown, the vessel follows the desired path with overall acceptable accuracy, consistent with the behaviour observed in the simulation tests. After each waypoint change, a noticeable overshoot occurs, primarily due to the limited yaw moment reserve of the vessel in the considered propulsion configuration, as noted earlier. In addition, a persistent lateral offset is observed, predominantly towards the south-west direction, which can be attributed to external disturbances. As a second general comment, it can be stated that the KPIs reported in Table 8 are generally higher than the corresponding simulated values reported in Table 5, as expected for an experimental test in a real environment subject to external disturbances.

Table 7. Speed components RMSE on a reference value.

Component	Ref value [m/s]	$RMSE_{KF}$	$RMSE_{Raw}$
V_x	0.42	0.035	0.25
V_y	−0.32	0.043	0.15

Going into more detail, the effectiveness of the coverage algorithm during the field experiments is evaluated, and, based on the statistical parameters of the path presented in Table 9, similar conclusions can be drawn to those from the surveillance simulation. Indeed, statistical quantities of the surveillance path make it very difficult to predict the future waypoints.

The experimental heatmap from Figure 8(a) by itself tells very little about the coverage of the AOI because of the reduced duration of the field experiment. However, a comparison with Figure 8(b), which shows the heatmap of the surveillance simulation in a time interval equal to the duration of the field experiment, makes it clear that in the field experiments, the coverage algorithm seems to perform better, even though a bias towards the centre of the AOI is still present.

Figure 8(c) shows the share of AOI covered over time during the field experiment and the surveillance simulation in the same time interval. As per the surveillance simulation, also in the field experiment, no hypotheses have been made on the perceptive sensor mounted on SWAMP. This figure suggests that the surveillance path generated during the field experiment allows faster coverage of the AOI than that generated in the simulation, covering 50% of the AOI in the same time interval, despite the 43%.

The analysis can therefore focus on pose-related errors, particularly the magnitudes of the cross-track error metrics MCTE and MaCTE. It can be observed that the MCTE is on the order of one metre, a value that falls within the grid cell used for domain discretisation and can be attributed to the lateral offset consistently observed towards the south-west along the entire path. Since this metric represents the primary KPI for the mission under consideration, its magnitude was deemed acceptable, and the mission objective can be considered fulfilled. As for the maximum cross-track error, its temporal evolution is reported in Figure 8(e), where a rapid decay can be observed following its peak. This behaviour is consistent with the limitations of the physical model discussed previously. For the MATE metric related to the along-track error, the same observations discussed in the previous subsection for the simulated results also apply to the experimental data.

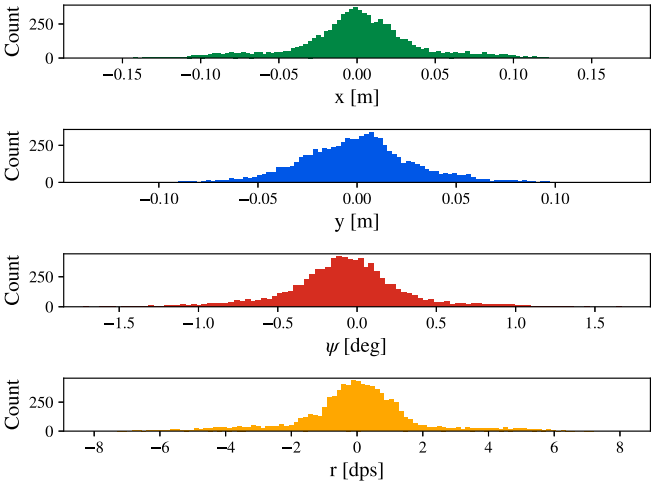

(a) Residuals distribution histograms.

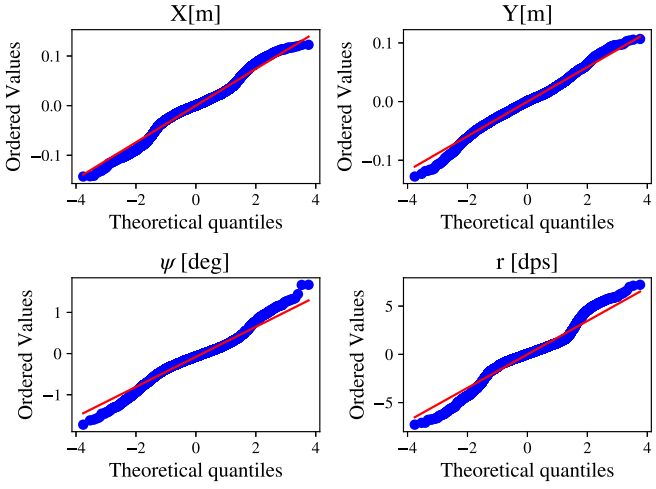

(b) Q–Q plot.

Figure 7. Residual analysis for each measure variable. (a) Residuals distribution histograms. (b) Q–Q plot.

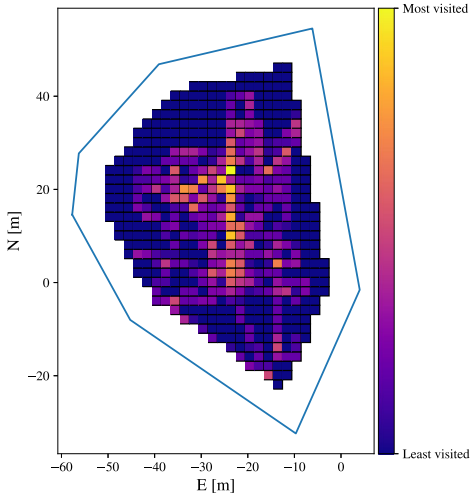

(a) Experimental Heatmap.

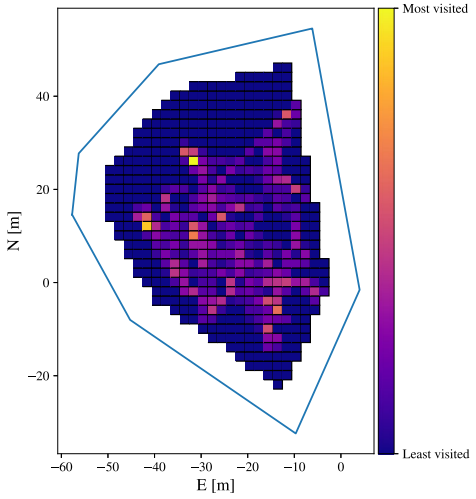

(b) Partial coverage heatmaps for the simulation.

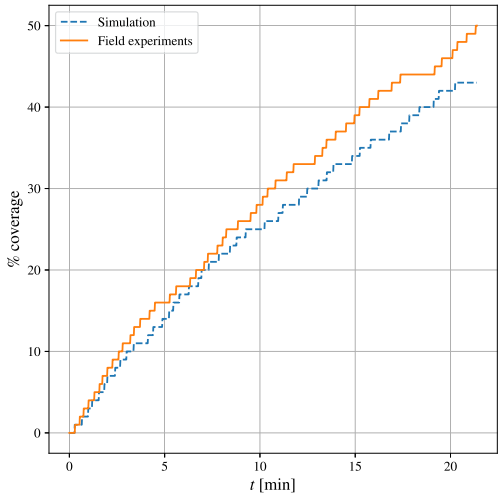

(c) Coverage over time during the surveillance simulation and field experiment in the same time interval.

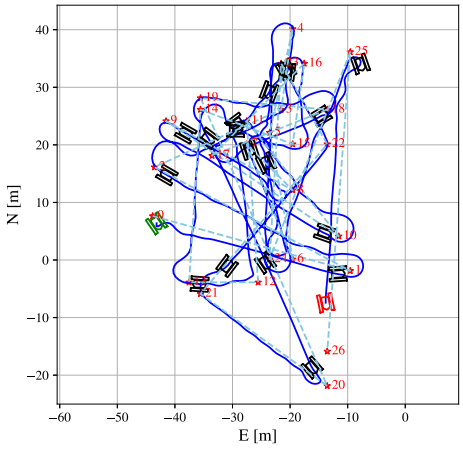

(d) Path.

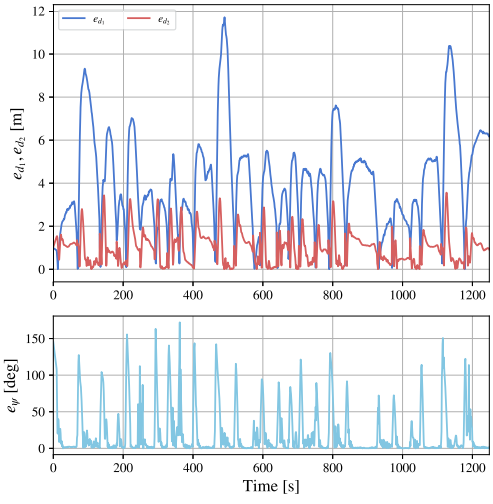

(e) Pose errors.

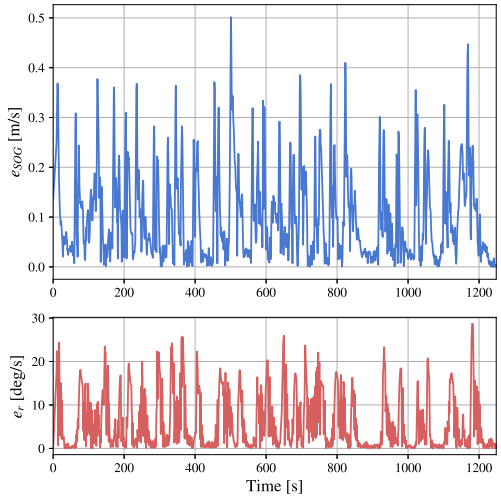

(f) Speed errors.

Figure 8. Experimental results. (a) Experimental Heatmap. (b) Partial coverage heatmaps for the simulation. (c) Coverage over time during the surveillance simulation and field experiment in the same time interval. (d) Path. (e) Pose errors and (f) Speed errors.

Table 8. Experimental Results – GNC performance.

MCTE [*m*]	*MaCTE* [*m*]	*MATE* [*m*]	*MPTE* [*deg*]	*MSOGE* [*m*/*s*]	*MROTE* [*deg*/*s*]
0.98	3.56	4	21	0.1	6

Table 9. Statistical parameters of the generated path in the field experiment.

Stat.	leg length [m]	course change [°]
Mean	23.44	116.3
Median	24.08	117.1
σ	8.913	32.47

Turning to the MPTE metric, which quantifies the heading error e_ψ, and observing its temporal evolution in Figure 8(e), it is evident that this metric is most affected by the transition from simulation to real-world testing. Indeed, the typical peak-and-decay pattern observed after each waypoint change shows absolute values similar to those in simulation but with a longer tail, which significantly increases the metric. Given the previously discussed physical limitations, this behaviour was expected and accurately reflects the vessel's limited yaw moment capability.

Finally, all the above observations also apply to the analysis of the velocity-related KPIs, namely MSOGE and MROTE. As expected and similarly to the previous cases, MSOGE assumes very small values, consistent with the temporal evolution of the speed error e_{SOG} shown in Figure 8(f). Conversely, MROTE exhibits higher values, with peaks occurring after each waypoint change. The difference relative to the simulation is primarily due to rotational errors, which extend beyond the transient peaks following waypoint changes and also include additional transients caused by external disturbances. The vessel is particularly sensitive to these disturbances due to its physical shape and large exposed surface area, especially with respect to wind, which affects the heading angle.

10. Conclusions and further research

This paper presents the validation of the enabling technologies underlying a MASS-based architecture for critical maritime infrastructure monitoring missions. The results demonstrate the correct operation of the proposed architecture and confirm the effective integration of its individual components. Both simulation and field tests validated the capability of the experimental platform to autonomously follow a surveillance path generated in real time by the coverage algorithm. In particular, the real-time integration and coordination of the physical platform, the control system, the surveillance path planner, and the state estimation module–based on onboard sensor data–were successfully demonstrated.

The results related to the state estimation system highlight its ability to acquire and process sensor data in real time at a stable update rate, ensuring reliable communication with the other subsystems. Furthermore, the analyses confirm the system's capability to provide a coherent and accurate estimate of the vessel state, both for directly measured variables and for those inferred through estimation techniques. The results for the coverage algorithm demonstrate the system's ability to effectively cover the Area of Interest (AOI), while also highlighting the stochastic nature of the generated paths and the resulting difficulty in predicting future waypoint locations. The tracking performance analysis shows overall reliable behaviour, while also revealing the main limitations of the current vessel configuration. The results confirm the physical constraints of the adopted MASS, which provides limited control capability in terms of moment and increases sensitivity to external disturbances.

Several solutions can be pursued to improve the overall system performance. These include addressing the vessel's physical limitations to improve force allocation and introducing curved paths near waypoints to better comply with the dynamic constraints of the SWAMP platform and to enhance tracking performance. In addition, future developments will focus on integrating these enabling technologies into the comprehensive surveillance architecture. The integration of the perception subsystem together with collision-free path planning and shadow vessel monitoring functionalities will constitute the subject of future work.

Acknowledgments

The authors would like to thank Mr. Lorenzo Berté, who made available the facility for the field experiments.

Disclosure statement

No potential conflict of interest was reported by the author(s).

Funding

This research was funded by European Union – NextGenerationEU. Piano Nazionale di Ripresa e Resilienza, Missione 4 Componente 2 Investimento 1.4 'Potenziamento strutture di ricerca e creazione di 'campioni nazionali di R&S' su alcune Key Enabling Technologies'. Code CN00000023 – Title: 'Sustainable Mobility Center (Centro Nazionale per la Mobilità Sostenibile – CNMS)'. However, views and opinions expressed are those of the author(s) only and do not necessarily reflect those of the European Union or European Commission. Neither the European Union nor the granting authority can be held responsible.

Declaration of generative AI and AI-assisted technologies in the writing

During the writing of this paper, the authors have made use of generative AI and AI-assisted technologies to improve the language and readability. The authors reviewed and edited as needed the generated text and take full responsibility for the content.

ORCID

C. Fruzzetti http://orcid.org/0000-0002-7447-6920
F. Ponzini https://orcid.org/0000-0002-3075-5274
N. Sabatino https://orcid.org/0009-0009-0147-8843
S. Donnarumma https://orcid.org/0000-0002-2889-6377
R. Zaccone https://orcid.org/0000-0002-5489-4498
M. Martelli https://orcid.org/0000-0003-1309-3464

References

Birk A et al. 2012. Cooperative cognitive control for autonomous underwater vehicles (CO3AUVs): overview and progresses in the 3rd project year. IFAC Proc Vol. 45(5):361–366. https://doi.org/10.3182/20120410-3-PT-4028.000603rd IFAC Workshop on Navigation, Guidance and Control of Underwater Vehicles.

Breivik M, Hovstein VE, Fossen TI. 2008. Straight-line target tracking for unmanned surface vehicles. Model Identif Control. 29(4):131–149. https://doi.org/10.4173/mic.2008.4.2

Bueger C. 2023. Russian Spy Ship in North Sea raises concerns about the vulnerability of key maritime infrastructures. https://theconversation.com/russian-spy-ship-in-north-sea-raises-concerns-about-the-vulnerability-of-key-maritime-infrastructure-204205.

Bueger C, Liebetrau T. 2023. Critical maritime infrastructure protection: what's the trouble? Mar Policy. 155:105772. https://doi.org/10.1016/j.marpol.2023.105772

Chataut R. 2024. Undersea cables are the unseen backbone of the global internet. https://theconversation.com/undersea-cables-are-the-unseen-backbone-of-the-global-internet-226300.

Claire JO. 2016. The ocean economy in 2030. In: Proceedings of the Workshop on Maritime Cluster and Global Challenges 50th Anniversary of the WP6. Vol. 1. Paris, France.

Clare M. 2021. Submarine clable protection and the environment. An update from the ICPC. https://www.iscpc.org/publications/submarine-cable-protection-and-the-environmentICPC_Public_EU_March%202021.pdf.

Clunie T, DeFilippo M, Sacarny M, Robinette P. 2021. Development of a perception system for an autonomous surface vehicle using monocular camera, lidar,

and marine radar. In: 2021 IEEE International Conference on Robotics and Automation (ICRA). p. 14112–14119.
Commission E. 2023. Eu wind power action plan. https://eur-lex.europa.eu/legal-content/EN/TXT/PDF/?uri = CELEX:52023DC0669.
de Kruif BJ. 2024. Autonomous docking of a feeder vessel. J Mar Eng Technol. 23(3):157–165. https://doi.org/10.1080/20464177.2023.2281742
De Wit C. 2009. Optimal thrust allocation methods for dynamic positioning of ships [master's thesis]. TU Delft.
Donnarumma S, Figari M, Martelli M, Zaccone R. 2020. Simulation of the guidance and control systems for underactuated vessels. Lecture notes in computer science (including subseries Lecture notes in artificial intelligence and lecture notes in bioinformatics). 11995 LNCS:108 – 119.
Donnarumma S, Martelli M, Vignolo S. 2015. Numerical models for ship dynamic positioning. p. 1078 – 1088.
Duan X, Bullo F. 2021. Markov chain–based stochastic strategies for robotic surveillance. Annu Rev Control Robot Auton Syst. 4(1):243–264. https://doi.org/10.1146/control.2021.4.issue-1
Elkins L, Sellers D, Monach WR. 2010. The autonomous maritime navigation (AMN) project: field tests, autonomous and cooperative behaviors, data fusion, sensors, and vehicles. J Field Robot. 27(6):790–818. https://doi.org/10.1002/rob.v27:6
Ferri G et al. 2017. Cooperative robotic networks for underwater surveillance: an overview. IET Radar Sonar Navig. 11(12):1740–1761. https://doi.org/10.1049/rsn2.v11.12
Fossen TI. 2011. Handbook of marine craft hydrodynamics and motion control. John Wiley & Sons.
Fritzon Å, Ljungkvist K, Boin A, Rhinard M. 2007. Protecting europe's critical infrastructures: problems and prospects. J Conting Crisis Manage. 15(1):30–41. https://doi.org/10.1111/jccm.2007.15.issue-1
Fruzzetti C, Buzzurro C, Donnarumma S, Martelli M. 2024a. Time domain design of a marine target tracking system accounting for environmental disturbances. J Mar Sci Eng. 12(11):2058. https://doi.org/10.3390/jmse12112058
Fruzzetti C, Martelli M, Lekkas A, Skjetne R, Breivik M. 2024b. Model-based motion control design for the milliampere1 prototype ferry. In: 2024 European Control Conference (ECC). p. 3636–3643.
González-Reolid I, Molina-Molina JC, Guerrero-González A, Ortiz FJ, Alonso D. 2018. An autonomous solar-powered marine robotic observatory for permanent monitoring of large areas of shallow water. Sensors. 18(10):3497. https://doi.org/10.3390/s18103497
He H, Van Zwijnsvoorde T, Lataire E, Delefortrie G. 2023. Model predictive controller for path following ships validated by experimental model tests. Ocean Eng. 288:115971. https://doi.org/10.1016/j.oceaneng.2023.115971
He Z et al. 2024. Dynamic domain-based collision avoidance system for autonomous ships: real experiments in coastal waters. Expert Syst Appl. 255:124805. https://doi.org/10.1016/j.eswa.2024.124805
Hinostroza M. 2025. Model identification, dynamic positioning, and thrust allocation system for the milliampere1 autonomous ferry prototype: field trial results. IEEE Access. 13:133609133609–133634. https://doi.org/10.1109/ACCESS.2025.3593251.
Johansen TA, Fossen TI. 2013. Control allocation–a survey. Automatica. 49(5):1087–1103. https://doi.org/10.1016/j.automatica.2013.01.035
Jouffray JB, Blasiak R, Norström AV, Österblom H, Nyström M. 2020. The blue acceleration: the trajectory of human expansion into the ocean. One Earth. 2(1):43–54. https://doi.org/10.1016/j.oneear.2019.12.016
Kantchev G. 2023. Sweden says second undersea cable damaged in Baltic Sea. https://www.wsj.com/world/europe/sweden-says-second-undersea-cable-damaged-in-baltic-sea-d9f21fea.
Kim J et al. 2024. Field experiment of autonomous ship navigation in canal and surrounding nearshore environments. J Field Robot. 41(2):470–489. https://doi.org/10.1002/rob.v41.2
Knights M. 2024. Assessing the Houthi War effort since October 2023. https://www.washingtoninstitute.org/policy-analysis/assessing-houthi-war-effort-october-2023.
Lou N et al. 2024. A robust gnss navigation method for usv in signal occlusion environment. IEEE Sens J. 24(17):27618–27630. https://doi.org/10.1109/JSEN.2024.3424551
Ludeno G, Esposito G, Catapano I, Soldovieri F, Gennarelli G. 2023. Short range k-band radar for maritime security. In: 2023 IEEE Conference on Antenna Measurements and Applications (CAMA). p. 30–33.
Manzari DTLBACRCV. 2020. Marine robots for underwater surveillance.
Martelli M, Faggioni N, Donnarumma S. 2020. A novel model based-design approach for a dynamic positioning system. In: Conference Proceedings of iSCSS.
Martinsen AB, Lekkas AM, Gros S. 2022. Reinforcement learning-based NMPC for tracking control of ASVs: theory and experiments. Control Eng Pract. 120:105024. https://doi.org/10.1016/j.conengprac.2021.105024
Maybeck PS. 1990. The Kalman filter: an introduction to concepts. New York, NY. Springer. p. 194–204.
Molina-Molina JC, Salhaoui M, Guerrero-González A, Arioua M. 2021. Autonomous marine robot based on ai recognition for permanent surveillance in marine protected areas. Sensors. 21(8):2664. https://doi.org/10.3390/s21082664
Nguyen T. 2023. The challenges of dark ships to the safety and security of commercial shipping and the way forward. Asia-Pac J Ocean Law Policy. 8(2):310–328.
Odetti A, Bruzzone G, Altosole M, Viviani M, Caccia M. 2020. SWAMP, an autonomous surface vehicle expressly designed for extremely shallow waters. Ocean Eng. 216:108205. https://doi.org/10.1016/j.oceaneng.2020.108205
Ponzini F, Fruzzetti C, Sabatino N. 2024. Real-time critical marine infrastructure multi-sensor surveillance via a constrained stochastic coverage algorithm. In: Conference Proceedings of iSCSS. Vol. 2024.
Ponzini F, Martelli M. 2025. Marine obstacles multi-modal detection, classification and tracking via camera-lidar late fusion. In: 2025 IEEE International Workshop on Metrology for the Sea; Learning to Measure Sea Health Parameters (MetroSea). p. 235–240.
Ponzini F, Van Hamme D, Martelli M. 2025a. Human detection in marine disaster search and rescue scenario: a multi-modal early fusion approach. Ocean Eng. 340:122341. https://doi.org/10.1016/j.oceaneng.2025.122341
Ponzini F, Zaccone R, Martelli M. 2025b. Lidar target detection and classification for ship situational awareness: a hybrid learning approach. Appl Ocean Res. 158:104552. https://doi.org/10.1016/j.apor.2025.104552
Simetti E, Turetta A, Torelli S, Casalino G. 2012. Civilian harbour protection: interception of suspect vessels with unmanned surface vehicles. IFAC Proc Vol. 45(27):435–440. https://doi.org/10.3182/20120919-3-IT-2046.000749th IFAC Conference on Manoeuvring and Control of Marine Craft.
Snyder JP. 1987. Map projections: a working manual. In: Professional paper. Vol. 1395. U.S. Government Printing Office.
Song R, Liu Y, Bucknall R. 2019. Smoothed A∗ algorithm for practical unmanned surface vehicle path planning. Appl Ocean Res. 83:9–20. https://doi.org/10.1016/j.apor.2018.12.001
Sørensen AJ. 2011. A survey of dynamic positioning control systems. Annu Rev Control. 35(1):123–136. https://doi.org/10.1016/j.arcontrol.2011.03.008
Tan CS, Mohd-Mokhtar R, Arshad MR. 2021. A comprehensive review of coverage path planning in robotics using classical and heuristic algorithms. IEEE Access. 9:119310–119342. https://doi.org/10.1109/ACCESS.2021.3108177
Tarasi L, Wanderlingh F, Noceti N, Indiveri G, Simetti E. 2024. Lidar and rgb camera performance for obstacle detection in marine environment. In: OCEANS 2024 – Halifax. p. 1–10.
Thombre S et al. 2022. Sensors and ai techniques for situational awareness in autonomous ships: a review. IEEE Trans Intell Transp Syst. 23(1):64–83. https://doi.org/10.1109/TITS.2020.3023957
Thyri EH, Bitar G, Breivik M. 2021. A 3 DOF path-following controller for a non-directionally stable vessel with slow thruster dynamics. IFAC-PapersOnLine. 54(16):288–294. https://doi.org/10.1016/j.ifacol.2021.10.10613th IFAC Conference on Control Applications in Marine Systems, Robotics, and Vehicles CAMS 2021.
UNCTAD. 2017. Review of maritime transport 2017. https://unctad.org/system/files/official-document/rmt2017_en.pdf.
UNCTAD. 2022. Review of maritime transport 2022. https://unctad.org/system/files/official-document/rmt2022_en.pdf.
Wang J et al. 2024. Real-sea validation of a model predictive controller's inherent robustness for medium-scale unmanned trimaran heading. Ocean Eng. 313:119513. https://doi.org/10.1016/j.oceaneng.2024.119513
Xia G, Wang G. 2016. Ins/gnss tightly-coupled integration using quaternion-based aupf for usv. Sensors. 16(8):1215. https://doi.org/10.3390/s16081215
Yasutomi AY, Fukushima EF. 2015. 2p1-d06 dynamical model identification of a catamaran type usv. In: The Proceedings of JSME annual Conference on Robotics and Mechatronics (Robomec). 2015.
Zaccone R. 2024. A dynamic programming approach to the collision avoidance of autonomous ships. Mathematics. 12(10):1546. https://doi.org/10.3390/math12101546
Zaccone R, Martelli M. 2018. A random sampling based algorithm for ship path planning with obstacles. In: Conference Proceedings of iSCSS.
Zaccone R, Ponzini F, Martelli M. 2026. Experimental validation of a modular navigation architecture for marine autonomous surface vehicles with reactive collision avoidance. Appl Ocean Res. 166:104903. https://doi.org/10.1016/j.apor.2025.104903
Zadeh SM, Abbasi A, Yazdani A, Wang H, Liu Y. 2022. Uninterrupted path planning system for multi-USV sampling mission in a cluttered ocean environment. Ocean Eng. 254:111328. https://doi.org/10.1016/j.oceaneng.2022.111328
Zhang W, Jiang F, Yang CF, Wang ZP, Zhao TJ. 2021. Research on unmanned surface vehicles environment perception based on the fusion of vision and lidar. IEEE Access. 9:63107–63121. https://doi.org/10.1109/ACCESS.2021.3057863